Size-Tuned ZnO Nanocrucible Arrays for Magnetic Nanodot Synthesis *via* Atomic Layer Deposition-Assisted Block Polymer Lithography

Chun-Hao Lin,[†] Srinivas Polisetty,[‡] Liam O'Brien,[‡,∥] Andrew Baruth,[‡,§] Marc A. Hillmyer,[*,†] Chris Leighton,[*,‡] and Wayne L. Gladfelter[*,†]

[†]Department of Chemistry, University of Minnesota—Twin Cities, Minneapolis, Minnesota 55455, United States, [‡]Department of Chemical Engineering and Materials Science, University of Minnesota—Twin Cities, Minneapolis, Minnesota 55455, United States, [§]Department of Physics, Creighton University, Omaha, Nebraska 68178, United States, and [∥]Cavendish Laboratory, University of Cambridge, Cambridge, CB3 0HE, U.K.

ABSTRACT Low-temperature atomic layer deposition of conformal ZnO on a self-assembled block polymer lithographic template comprising well-ordered, vertically aligned cylindrical pores within a poly(styrene) (PS) matrix was used to produce nanocrucible templates with pore diameters tunable *via* ZnO thickness. Starting from a PS template with a hexagonal array of 30 nm diameter pores on a 45 nm pitch, the ZnO thickness was progressively increased to narrow the pore diameter to as low as 14 nm. Upon removal of the PS by heat treatment in air at 500 °C to form an array of size-tunable ZnO nanocrucibles, permalloy ($Ni_{80}Fe_{20}$) was evaporated at normal incidence, filling the pores and creating an overlayer. Argon ion beam milling was then used to etch back the overlayer (a Damascene-type process), leaving a well-ordered array of isolated ZnO nanocrucibles filled with permalloy nanodots. Microscopy and temperature-dependent magnetometry verified the diameter reduction with increasing ZnO thickness. The largest diameter (30 nm) dots exhibit a ferromagnetic multidomain/vortex state at 300 K, with relatively weakly temperature-dependent coercivity. Reducing the diameter leads to a crossover to a single-domain state and eventually superparamagnetism at sufficiently high temperature, in quantitative agreement with expectations. We argue that this approach could render this form of block polymer lithography compatible with high-temperature processing (as required for technologically important high perpendicular anisotropy ordered alloys, for instance), in addition to enabling separation-dependent studies to probe interdot magnetostatic interactions.

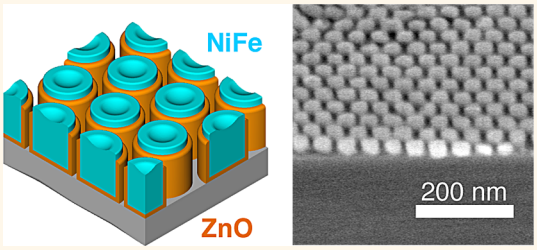

KEYWORDS: atomic layer deposition · block copolymer · nanolithography · bit patterned media · nanocrucible · magnetic nanodots

The preparation of large-area, nanoscale features from block copolymer (BCP)-derived thin film templates is being actively pursued as an attractive nanolithographic technique.[1−9] Block copolymers can adopt spherical, cylindrical, lamellar, or bicontinuous morphologies with periodicities on length scales of tens of nanometers,[10] in thin films atop a variety of substrates. Used in combination with graphoepitaxy or chemoepitaxy the self-assembly of BCP films can even be guided into well-defined arrays of lines, cylinders, or dots with potential use in the preparation of magnetic storage media,[11−14] nanowire arrays,[15,16] and integrated circuits.[17−19]

In the field of magnetic data storage, for example, bit patterned media (BPM) offers an exciting potential alternative to the use of continuous, granular films of ferromagnetic material.[12−14] In BPM each isolated ferromagnetic island stores a single bit of information, and thus exceeding the 1 Tb/in.[2] threshold requires islands in a square array to have periodicities below 25 nm, a range that is accessible to BCP templates. Ferromagnetic nanodot arrays inspired by such applications have been prepared from self-assembled BCP templates using a wide variety of both subtractive and additive lithographic processes.[12−14] An early example of a subtractive lithographic method involved forming an ordered template from sphere-forming poly(styrene)-*block*-poly(ferrocenyldimethylsilane) (PS-*b*-PFS).[11] Reactive ion etching with an oxygen plasma removed the PS and left a

* Address correspondence to wlg@umn.edu (W. L. Gladfelter), leighton@umn.edu (C. Leighton), hillmyer@umn.edu (M. A. Hillmyer).

Received for review October 8, 2014 and accepted January 20, 2015.

Published online January 20, 2015
10.1021/nn505731n

pattern of silicon–iron-oxide nanodots that was ultimately transferred to an underlying cobalt film in a final ion milling step. More recently, a modified atomic layer deposition (ALD) process was used to selectively alter one of the blocks of a BCP template to enhance the contrast between the blocks in the important pattern transfer step.[8,20–24] By a process referred to as sequential infiltration synthesis (SIS), Elam, Darling, and co-workers exposed phase-separated BCP films, typically poly(styrene)-*block*-poly(methyl methacrylate) (PS-*b*-PMMA), to alternating gas pulses of trimethylaluminum (TMA) and water. The more polar PMMA block absorbed the reactants more rapidly than the nonpolar PS block. The aluminum oxide that formed selectively within the PMMA block increased its plasma etch resistance, thus allowing it to serve as a mask capable of transferring sub-20 nm features to the underlying substrate in a subtractive lithographic process.[24]

In a relatively early example of an additive process, an initial PS-*b*-PMMA template having an array of perpendicular PMMA cylinders was etched to remove the PMMA, leaving an array of holes within the PS mask that was coated with cobalt metal. Removal of the PS mask left an array of isolated cobalt nanodots.[25] In a more recent example, solvent vapor annealing (SVA)[26] was used in conjunction with poly(styrene)-*block*-poly(lactide) (PS-*b*-PLA) thin films to produce well-ordered, perpendicular, cylindrical nanotemplates with lateral correlation lengths up to 6.9 μm and low areal defect densities.[27] Following chemical removal of the PLA block, a Damascene-type approach (where the template is overfilled with excess magnetic material and etched back to form nanodot arrays) was used for pattern transfer to magnetic nanodot arrays.[27,28] Such approaches offer a number of advantages over conventional "lift-off"-style patterning methods.[25,29]

In the examples noted above involving template formation by removal of the minority component, the final feature sizes are simply dictated by the domain sizes in the original block polymer template. Moon *et al*. described the use of aluminum oxide ALD to achieve pattern multiplication of lines in nanoporous PS templates formed using traditional PS-poly(methyl methacrylate) block polymer thin films. The Al_2O_3 was subsequently used as an etch-block to form silicon nanowires or nanotubes atop the underlying substrate.[30] Here we describe a method where ALD, a technique with the ability to coat complex surfaces conformally, is used to decrease the inner diameter of the cylindrical pores formed from a highly ordered BCP template, forming an inorganic oxide "nanocrucible" array. The fact that the oxide film thickness is directly correlated with the number of ALD cycles (as in ALD of Al_2O_3 and ZnO on anodic Al_2O_3 with hexagonal arrays of 65 nm diameter pores[31,32]) provides tunability of the pore diameter with subnanometer resolution.[31] We use this approach, in conjunction with a Damascene-type process, to produce hexagonally packed $Ni_{80}Fe_{20}$ (permalloy, Py) nanodot arrays of approximate diameter 19 and 14 nm from a single PS-*b*-PLA BCP template with an original PLA cylinder diameter of 30 nm and a center-to-center spacing of 45 nm. The volume reduction was confirmed by temperature-dependent magnetometry, which verified both the expected multidomain/vortex state to single-domain crossover and the onset of superparamagnetism, in quantitative agreement with established phase diagrams and simple estimates. In addition to providing a facile means to tune edge-to-edge spacing at fixed pitch in order to study interdot magnetostatic interactions, our method potentially renders lift-off and Damascene-style BCP lithography compatible with high-temperature processing (by replicating the BCP pattern in ZnO), as required for technologically important materials such as $L1_0$ ordered alloys (*e.g.*, FePt) with large perpendicular magnetic anisotropy.

RESULTS AND DISCUSSION

Overview. Scheme 1 illustrates the fabrication process to prepare size-tunable ZnO nanocrucible templates for use in magnetic nanodot production, with individual steps described in more detail in the Methods section. The initial polymer template (60 nm thick) is formed by spin coating the PS-*b*-PLA onto Si wafers rendered hydrophobic by treatment with hexamethyldisilazane. After a solvent vapor annealing process,[26,27] the 2-D hexagonal close-packed cylinder array is treated with dilute base to remove the PLA component, leaving 30 nm diameter cylindrical pores aligned perpendicular to the substrate surface. Prior to ALD of ZnO, the structures were exposed to a brief oxygen plasma etch to ensure that no organic wetting layer remains at the bottom of the pores; step I in Scheme 1 illustrates the result to this point in the process. ZnO films are then deposited *via* ALD (more details provided below) to produce a secondary template that is essentially a thin ZnO conformal coating (see step II in Scheme 1). The resultant pore size of this secondary template is directly controlled by the thickness of the ALD layer (*i.e.*, the number of ALD cycles). Calcination of the template at 500 °C in air removes the PS, leaving the ZnO secondary template (which we refer to as the nanocrucible array) behind (step III). Critically, the ZnO retains the morphology of the initial PS template after this step. A Damascene-type process is then used to produce the Py nanodot array. In this process, the ZnO template is overfilled with Py by evaporation (step IV) and the overlayer is then removed with normal incidence Ar ion beam milling, etching back the Py to expose the ZnO template (step V). This scheme results in a well-defined ZnO nanocrucible array, with each nanocrucible filled with Py (step V).

Illustrating the successful execution of this Scheme, Figure 1 shows plan view and cross-sectional

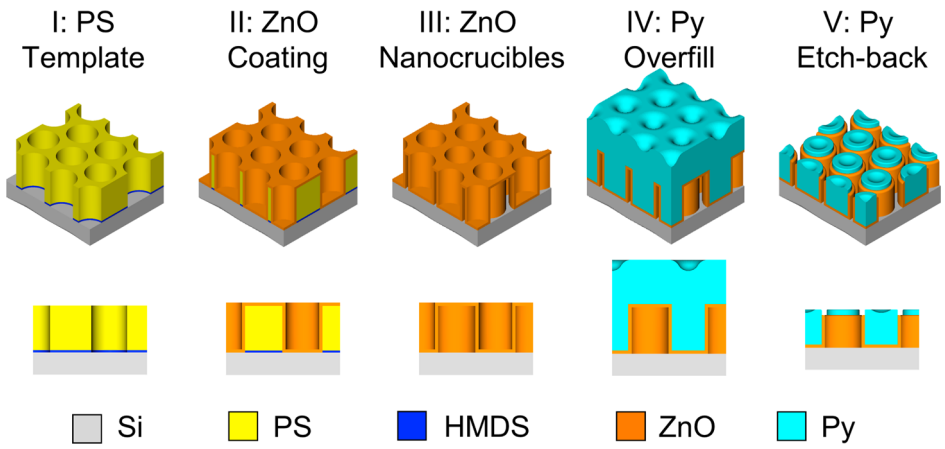

Scheme 1. Schematic representation of the size-tunable template fabrication process for magnetic nanodot array production. (I) Self-assembled poly(styrene) (PS) template with hexagonally packed cylindrical pores that traverse the entire film thickness. (II) Conformal coating of ZnO over the PS. The pore size is tuned by ZnO thickness. (III) Calcination at 500 °C removes the PS template, leaving a thermally stable ZnO mask with a similar morphology to I; we refer to this structure as a "nanocrucible" array. (IV) Normal incidence permalloy (Py) deposition into the hard mask using e-beam evaporation, overfilling the template pores. (V) Permalloy overlayer and ZnO surface layer removal *via* normal incidence Ar ion beam milling, resulting in well-ordered ZnO nanocrucibles, of varying inner diameter, containing the permalloy magnetic nanodot array.

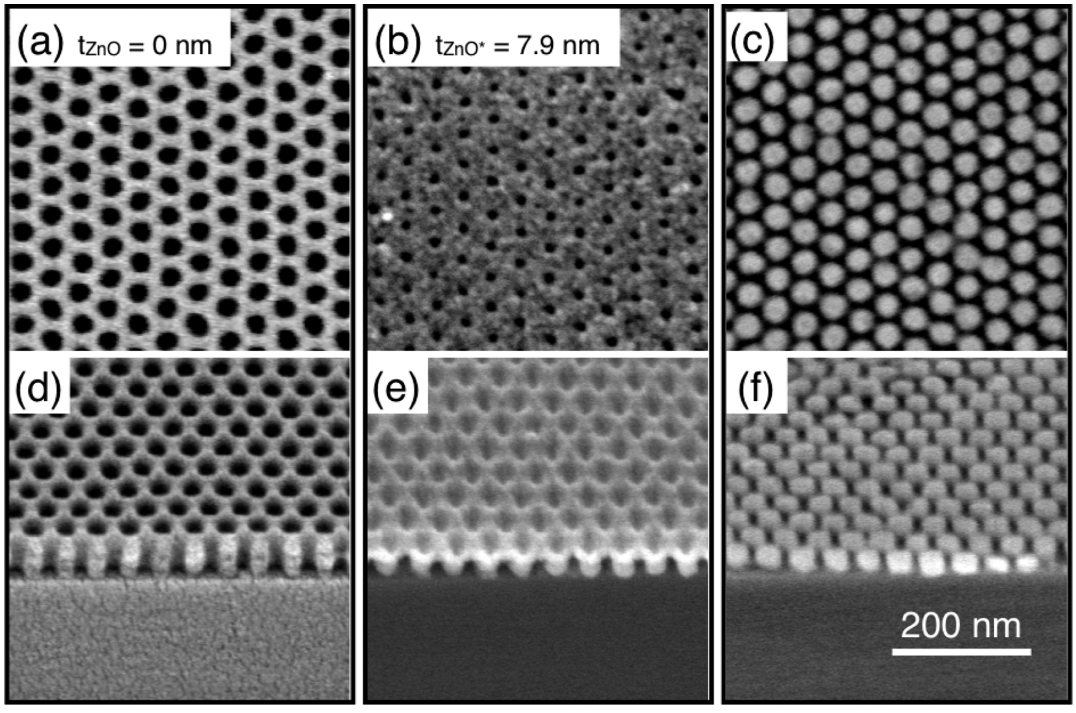

Figure 1. Plan-view (a–c) and cross-sectional (tilted to ~30° above the substrate surface) (d–f) scanning electron micrographs of the poly(styrene) template (a and d, with a 3 nm platinum coating for imaging), ZnO secondary template (b and e) with a true ZnO thickness, t_{ZnO^*} (see text for definition) of 7.9 nm (240 ALD cycles), and the resultant ZnO nanocrucibles containing permalloy nanodots (c and f).

(tilted ~30° above the substrate surface) scanning electron microscopy (SEM) images following initial formation of the highly ordered polymer template (Figure 1a and d), after 240 ZnO ALD cycles (Figure 1b and e), and following both Py deposition and ion milling (Figure 1c and f). Successful reduction in pore diameter is clear from comparing Figure 1a and b, while Figure 1c and f reveal formation of a well-ordered Py nanodot array. Note that the images in Figure 1c and f depict both the Py nanodot *and* the surrounding ZnO shell (nanocrucible); weak contrast between the two may be visible. Also important, Figure 1d confirms that the nanopores in the PS span the entire thickness of the film, persisting to the Si substrate, consistent with our prior work.[27,28]

The following sections of this paper describe in detail the formation of the secondary ZnO template (*i.e.*, steps II and III in Scheme 1), the deposition of Py

(step IV), the ion milling (step V), and the magnetic properties of the resulting nanodot arrays. Three different nanodot arrays, which we name as the 30, 19, and 14 nm arrays based on the approximate mean diameter of the ZnO pores, and thus the final Py nanodots, will be presented. The 30 nm array was prepared as described previously,[27,28] using only the initial PS template (*i.e.*, no ALD process). For this sample steps II and III in Scheme 1 were thus eliminated, and the nanodots are contained within PS rather than ZnO nanocrucibles.

Zinc Oxide ALD. A common approach to depositing ZnO by ALD involves exposure of the substrate to alternating pulses of diethylzinc ($Zn(C_2H_5)_2$) and H_2O, separated by N_2 purge pulses.[31] Initial attempts using these reactants on PS-coated Si substrates resulted in discontinuous films. By changing the oxygen source from H_2O to O_3, however, reproducible formation of smooth ZnO films was obtained. Ozone has been shown to react slowly with PS surfaces, causing an increase in oxidized functional groups on the PS surface.[33] This may provide additional sites for reaction with $Zn(C_2H_5)_2$ during the early stages of ALD, leading to more uniform films. To verify that O_3 does not lead to extensive degradation or etching of the PS film, a 36 nm thick uniform PS film on Si was exposed to a typical ALD pulse sequence in our reactor maintained at 85 °C (below the glass transition temperature of bulk PS), but without the $Zn(C_2H_5)_2$, for 200 cycles. Grazing incidence X-ray reflectivity (GIXR) before and after indicated no obvious changes in film thickness, density, or surface roughness (see Supporting Information Figure S1).

The ZnO films in this study were deposited at 85 °C using a pulse sequence of $Zn(C_2H_5)_2$ (4 s), N_2 (5 s), O_3 (8 s), and N_2 (5 s). From GIXR measurements of the thickness of films grown on Si substrates (Supporting Information Figure S2), the above conditions were found to produce an increment of 0.050 nm/cycle for as-deposited films (Figure 2). For context, note that previous publications on ZnO ALD using $Zn(C_2H_5)_2$ and O_3 as precursors reported thickness/cycle values

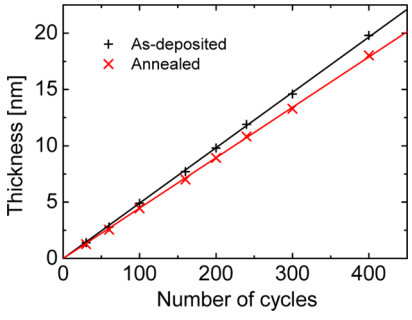

Figure 2. ZnO film thickness *vs* number of ALD cycles. The substrates were silicon, and GIXR was used to measure the film thickness. The black + symbols correspond to as-deposited films, and the red × symbols correspond to the thermally annealed films. The lines are straight-line fits through the origin.

of 0.17 nm/cycle at 250 °C.[34,35] Despite our (enforced) operation below the optimum temperature window for the ZnO ALD process, the film thickness nevertheless exhibits an excellent linear correlation with the number of cycles out to 400 (the largest number prepared), as shown in Figure 2. Annealing these test films in air at 500 °C for 30 min results in a 10% densification based on the change in film thickness. Thus, the thickness/cycle for such annealed films was determined to be 0.045 nm/cycle (also shown in Figure 2).

On the basis of X-ray diffraction, the as-deposited ZnO films were amorphous, perhaps unsurprising given the low deposition temperature. No carbon was found in the films *via* Rutherford backscattering spectrometry, however, due to the efficient conversion of the zinc-ethyl groups into acetaldehyde during ozone pulses.[34] In contrast to the as-deposited case, films annealed at 500 °C in air exhibited clear Bragg reflections consistent with the wurtzite crystal structure of ZnO (see Supporting Information Figure S3). In the templated films, this high temperature annealing also serves to decompose the underlying PS template. The result, as represented in step III of Scheme 1, is a ZnO-coated substrate having a hexagonal array of cylindrical pores (nanocrucibles), with diameter (d_{pore}) dependent on the original PS template diameter (d_{PS}) and the nominal deposited thickness of ZnO (t_{ZnO}). Under the assumption of perfect conformality of the ZnO deposition, we anticipate $d_{pore} = d_{PS} - 2t_{ZnO}$, an expectation that is analyzed below.

SEM (Figure 3) and subsequent image analysis using the ImageJ package (see Supporting Information Figure S4 for details) were used to determine more precise d_{pore} values for the nominally 30, 19, and 14 nm templates, of 29.8 ± 2.1, 18.5 ± 1.6, and 14.1 ± 2.2 nm, respectively. Note that for the PS-only case (no ZnO), a thin Pt layer was sputtered (see Methods for details) to enhance imaging; this was assumed to have a negligible effect on d_{PS}. The reported errors here represent one standard deviation (Δd_{pore}), and the relatively narrow distributions ($\Delta d_{pore}/d_{pore}$ from 7.0% to 16%) are apparent from the histograms shown as insets in Figure 3a–c. Considering these three templates in turn, Figure 3a depicts the 30 nm array ($t_{ZnO} = 0$), while Figure 3b and c show templates after 100 and 240 ZnO ALD cycles, followed by a 500 °C calcination in air. These two arrays thus have nominal deposited ZnO thicknesses, t_{ZnO}, of 4.5 and 10.8 nm, respectively, using the relationship established in Figure 2. Using $d_{pore} = d_{PS} - 2t_{ZnO*}$, where t_{ZnO*} is the *true* value of the ZnO coating thickness inside the pore, as deduced from measured values for d_{pore} and d_{PS}, results in $t_{ZnO*} = 5.7$ and 7.9 nm, respectively, for the 19 and 14 nm arrays. While the t_{ZnO*} and t_{ZnO} values are thus relatively close, the 30% deviations between these values may indicate some departure from the assumption of perfect conformality under our growth

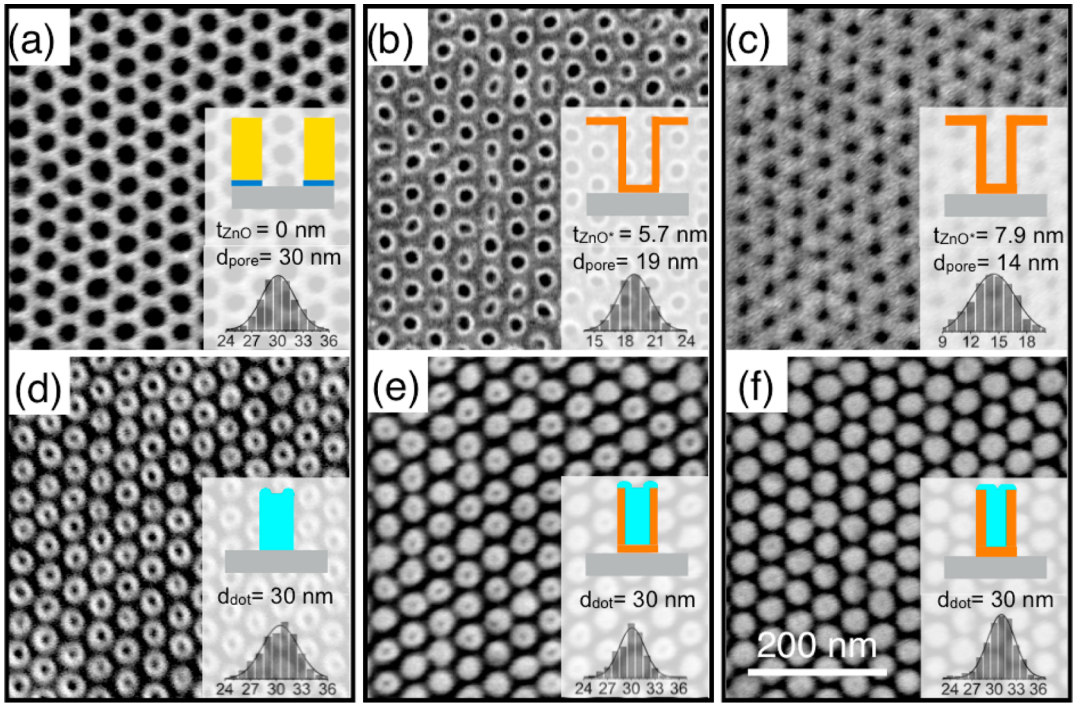

Figure 3. Plan-view SEM images of templates (a−c) and the subsequent filled nanocrucible arrays (d−f) following the Damascene process described in the text. Insets show schematic depictions of single features (the colors correspond with Scheme 1), as well as histograms with Gaussian fits of feature size distributions. The histograms are based on analysis of an average of 1300 features. (a−c) Each begin with an identical PS template coated to a true ZnO thickness, t_{ZnO*} (see text for definition), of (a) 0 nm, (b) 5.7 nm, and (c) 7.9 nm. The pore diameters are 29.8 ± 2.1, 18.5 ± 1.6, and 14.1 ± 2.2 nm, respectively. (d−f) Equivalent images after the ZnO nanocrucibles are filled with permalloy and etched back in a "Damascene-type" process. The feature diameters (permalloy dot plus ZnO shell) are 29.8 ± 2.1, 29.6 ± 2.2, and 30.3 ± 2.1 nm, respectively. In all cases, the error bars indicate one standard deviation.

conditions. In any case, Figures 1 and 3 clearly illustrate successful diameter reduction using ZnO ALD, with pore sizes as low as 14 nm, *i.e.*, half the original template diameter.

Permalloy Deposition and Ion-Bean Milling. Using normal incidence ultra-high-vacuum electron beam evaporation, Py was deposited from an alloy source onto each of the templates shown in Figure 3a−c at a rate of 3 nm/min and at a substrate temperature of 23−27 °C. (We have previously demonstrated successful filling of 25 nm pores by this method.[28]) The templates were intentionally overfilled to a nominal thickness of 70 nm, resulting in the dimpled surface structure indicated in panel IV of Scheme 1. Using a Damascene-type approach, the excess Py overlayer was then etched back using normal incidence Ar ion beam milling. This leads to planarization and, eventually, exposure of the ZnO (or PS in the t_{ZnO} = 0 case, Figure 3a). At this point the similarity of the Ar ion milling rates for Py (3.2 nm/min) and ZnO (3.8 nm/min) results in the formation of an array of Py cylinders contained within ZnO nanocrucible shells (Figure 3e,f). This process was monitored by SEM imaging after multiple etch durations (see Supporting Information Figure S5) in order to establish appropriate etch times. The final results are shown in Figures 3d−f, where high-fidelity pattern transfer and the formation of well-ordered isolated nanodot arrays are clear in each case. Note that after certain degrees of Ar ion milling occasional "bridges" between ZnO nanocrucibles were observed, although these could be almost completely eliminated by further milling. Supporting Information Figure S6 shows clear examples, and they can also be seen at certain locations in Figure 3e.

When examining the fine details of the images shown in Figure 3d−f, two additional issues must be considered. First, it is important to appreciate that little contrast exists between the Py nanodots and ZnO perimeters in the secondary electron SEM imaging shown in Figure 3e and f. The measured average dot diameters in Figure 3d−f, which are 29.8 ± 2.1, 29.6 ± 2.2, and 30.3 ± 2.1 nm, respectively, thus correspond to Py nanodot plus ZnO nanocrucible shell and are therefore close to the original nominal PS pore size of 30 nm. Further evidence for the ZnO crucible structures following the Py deposition and ion beam milling is shown in a cross-sectional SEM of a fractured sample (Figure S7 in the Supporting Information). As discussed in more detail in the next section, magnetometry measurements provide additional verification of the decreasing Py dot diameter. Second, Figure 3d, and to a lesser extent Figure 3e, show that the surfaces of the nanodots have an apparent ring shape. While some contribution from well-known SEM imaging artifacts

should not be ignored, it is likely that this reflects a degree of "atoll" shape to the Py nanodots resulting from the Damascene process, as suggested in image V in Scheme 1. In essence the dimpled surface present following Py deposition, as shown in Figure S5(a), is not fully planarized by the ion milling process for the larger diameter nanodots. For the smallest diameter Py nanodots, the plan view SEM in Figure 3f and the cross-sectional SEM shown in Figure 1f show little evidence for the atoll shape. As the original pore diameter increases, the plan view SEMs in Figure 3d and e show that the final nanodots exhibit the atoll surface to an increasing extent. The cross-sectional SEM, Figure S8, of a closely related sample provides additional support for the shape of the Py dots at the end of the process.

Magnetic Characterization. To assess the quality of the nanodots derived from our process and to further confirm the anticipated Py diameter decrease in the arrays shown in Figures 3e,f, we performed temperature-dependent magnetization hysteresis loop measurements. These enable assessment of the location of our dot arrays on previously established phase diagrams for Py,[36,37] as well as determination of their thermal stability; these are both direct probes of dot volume and aspect ratio. Such measurements were performed on arrays with Py dot heights (from calibrated Ar milling rates and direct GIXR measurements) of 30 nm. The results are shown in Figure 4a–c, where the magnetization normalized to its value in a 1 T field (M/M_{1T}) is plotted as a function of in-plane applied field (H), at temperatures of 20 and 300 K, for Py dot arrays with expected diameters (d_{dot}) of 30, 19, and 14 nm (Figure 3d–f). The hysteresis loops were acquired to 1 T or beyond, but are plotted here to only 0.3 T to illustrate the low H behavior.

Starting with the 30 nm diameter dots (Figure 4a), we find a hysteresis loop indicative of ferromagnetism at 300 K. The saturation magnetization is 50–60% of bulk, demonstrating relatively high quality patterning with low etch damage.[28] The most striking feature at 300 K is the "pinched" $M(H)$ loop, the width at $M = 0$ being considerably smaller than at $M/M_{1T} = \pm 0.75$. One simple interpretation is a multidomain/vortex state, which is known to result in pinched loops, ideally displaying zero remanance and coercivity. Departures from this ideal shape, as seen in the current case, are common.[38] In fact, placing these nanodots on the established magnetic phase diagram for cylindrical Py dots in the height-diameter plane,[37] we find that at height 30 nm and diameter 30 nm (around 5.3 exchange lengths for Py[37]) such a multidomain/vortex state is exactly the expected behavior. On cooling from 300 K to 20 K the coercivity (H_C) is found to increase only weakly (by a factor of 5), as expected for thermally stable ferromagnetic dots. The signatures of a vortex state are lost, however, the 20 K $M(H)$ loop showing no obvious pinching, ascribable to the thermally driven single domain to vortex transition previously seen in Fe

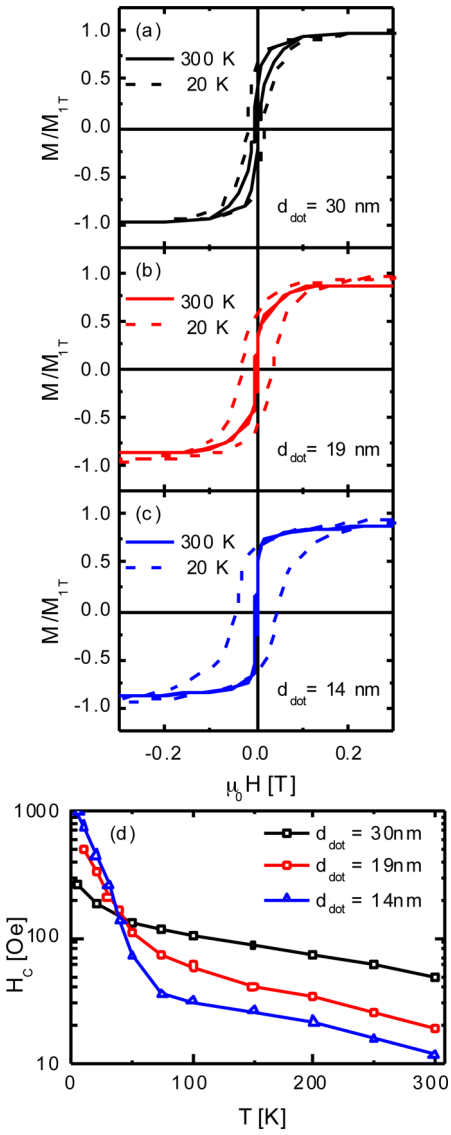

Figure 4. Background-subtracted magnetization normalized to the 1 T value (M/M_{1T}) *vs* in-plane applied magnetic field, $\mu_0 H$, at T = 20 K (dashed lines) and 300 K (solid lines) for permalloy nanodot arrays with a fixed dot height of 30 nm and approximate diameters (d_{dot}) of (a) 30 nm, (b) 19 nm, and (c) 14 nm. (d) T dependence of the coercivity (H_C) in each case. The $M(H)$ hysteresis loops shown have had the high-field slope subtracted as an approximation to background subtraction. This background arises mostly due to the Si substrates.

nanodots.[38] The temperature dependence of H_C from multiple isothermal $M(H)$ loops is shown explicitly in Figure 4d, where it can be seen that $H_C(T)$ for these 30 nm diameter dots is monotonic and featureless. The magnetic properties of the 30 nm diameter array are thus consistent with the thermally stable ferromagnetic properties expected from prior work. To further support this, we calculated the expected blocking temperature for such dots, using the appropriate measurement time scale, a 1 GHz attempt frequency, the measured height, diameter, and saturation magnetization, and a simple estimate of anisotropy based on in-plane coherent switching (from the measured

coercivity). The calculated blocking point in this case (620 K) significantly exceeds room temperature, consistent with our observation of thermally stable ferromagnetism at 300 K.

At 19 nm dot diameter (Figure 4b), the behavior is distinctly different. Specifically, while the 20 K data show ferromagnetism with relatively high H_C and remanance, at 300 K we find a near closed loop with very low remanance. As shown in Figure 4d, $H_C(T)$ is very different than the 30 nm case, decreasing by a factor of 25 on warming, with some indication of a change in slope near 150 K. We interpret these observations, simply, in terms of a single-domain ferromagnetic state at 20 K with a superparamagnetic blocking point of around 150 K. The single-domain state is indeed consistent with expectations from the phase diagram for Py, where 19 nm diameter dots (3.3 exchange lengths) of this height lie close to the "triple point" where "multidomain/vortex", "single-domain in-plane", and "single-domain perpendicular" meet. Similar calculations to those discussed above result in a predicted blocking temperature for these 19 nm diameter dots of 130 K, in reasonable agreement with the estimate from experiment of 150 K. It must be emphasized that we are postulating here a blocking temperature of 150 K for the *average* dot in this array. Statistical distributions in diameter, height, shape, magnetocrystalline anisotropy, and saturation magnetization must generate a distribution in blocking points. This accounts for the lack of a sharp up-turn in $H_C(T)$ in Figure 4d, as well as the finite H_C even above the postulated 150 K average blocking point.

At a dot diameter of 14 nm (Figure 4c), the behavior is again altered. The 20 K hysteresis loop still indicates ferromagnetism, but the 300 K $M(H)$ data reveal an almost closed loop, with little remanance and very low H_C. As shown in Figure 4d, H_C in fact decreases by a factor of 100 on warming from 20 to 300 K, with a distinct change in slope at 75 K. Following our analysis for the 19 nm dot array, we interpret this in terms of single-domain ferromagnetism at 20 K, giving way to superparamagnetism at an average blocking temperature of 75 K. Our calculated blocking temperature in this case is 47 K, again in reasonable agreement with experiment, particularly given the approximations made in our estimates, which ignore factors such as surface effects, nonidealities in shape, size distributions, *etc*. On this topic we mention parenthetically that these Py nanodot arrays are uncapped and that their oxidation does result in some exchange biasing effects at low temperatures, particularly below 30 K. This is apparent from close examination of the 20 K data in Figure 4a–c, where a slight loop shift occurs. As a final comment on the data of Figure 4, specifically Figure 4d, we note that the inversion of the H_C trend with dot diameter at low and high temperatures provides a clear illustration of the arguments made with respect to thermal stability. At low temperatures (below about 50 K), H_C increases with decreasing diameter, as expected for thermally stable ferromagnetic dots entering a single-domain state. At high temperatures on the other hand (above about 50 K), H_C decreases with decreasing diameter, reflecting the loss of thermal stability and decrease in blocking temperature. In short, the diameter-dependent magnetic properties of these nanodot arrays are in reasonable agreement, both qualitatively and quantitatively, with expectations based on established phase diagrams and thermal stability estimates for Py. Note that we have ignored interdot interaction effects in the analysis presented here. Even in the 30 nm diameter case (where dipolar interactions are strongest), micromagnetic simulations indicate nearest neighbor stray fields that may play a minor role at room temperature, but are negligible at 20 K; observation of a multidomain/vortex state renders these fields even less important.

CONCLUSIONS

In summary, through a combination of block copolymer self-assembly, solvent vapor annealing, and low-temperature atomic layer deposition, we have demonstrated successful lithography of highly ordered large-area arrays of size-tuned ZnO nanocrucibles in the 14–19 nm diameter range. The precise thickness control and conformality of atomic layer deposition enable fine-tuning of pore diameters to values up to a factor of 2 smaller than the original block polymer template. Using a Damascene-type approach, these templates were then used for high-fidelity synthesis of highly ordered magnetic metal nanodot arrays. Diameter reduction by this atomic layer deposition assisted process was verified through temperature-dependent magnetization measurements, which show the expected crossovers from multidomain/vortex states to single domain, and eventually to a superparamagnetic state at sufficiently high temperatures. We suggest that this approach could enable detailed investigations of interdot magnetic interactions at a fixed pitch, in addition to lift-off and Damascene-style block polymer lithography compatible with high-temperature processing. The latter is of technological relevance for bit patterned media based on high perpendicular anisotropy ordered metallic alloys.

METHODS

The nanoporous PS template was prepared using our established protocol (described elsewhere[27]) consisting of spin coating a 60 nm thick film of PS-*b*-PLA (M_n = 69 kg mol^{-1}, Đ = 1.09, f_{PLA} = 0.28) from a 1.7% (w/v) toluene solution at 3000 rpm onto a hydrophobically modified silicon wafer. The films were

then immediately diced into approximately 5 mm × 5 mm pieces and thermally treated in an 85 °C gravity convection oven for at least 1 h. In this step, an 8% decrease in film thickness was observed, on average, with minimal changes beyond this initial 1 h period, implying some initial removal of trapped volatiles after spin-casting. Climate-controlled SVA of the PS-*b*-PLA films in tetrahydrofuran (THF) vapor for 15 min resulted in a highly organized arrangement of cylindrical PLA domains that were hexagonally packed and perpendicularly aligned to the substrate surface in a continuous PS matrix. The resultant films were immediately immersed in a 0.05 M NaOH solution (H_2O/CH_3OH = 6:4 by volume) for 45 min to remove the PLA minority component, resulting in a nanoporous PS template. The samples were then transferred into a cosolvent of H_2O/CH_3OH = 6:4 by volume for ~3 min to wash the NaOH from the samples. As previously demonstrated, the presence of a thin wetting layer of PS at the HMDS-treated substrate surface is possible.[26−29] Thus, the films were also subjected to a 10 s O_2 plasma etch to remove any additional material at the substrate surface within the pores.

ZnO was deposited *via* atomic layer deposition at 85 °C, sufficiently below the glass transition temperature of PS (~100 °C). The pulse sequence consisted of $Zn(C_2H_5)_2$ (4 s), N_2 (5 s), O_3 (~2% in O_2, 8 s), and N_2 (5 s). Throughout the deposition the $Zn(C_2H_5)_2$ precursor vessel was cooled to −15 °C. Using these conditions the deposition thickness/cycle was calibrated on a bare silicon wafer (see Figure 2 and Supporting Information Figure S2). The deposition rate was 0.05 nm/cycle. For comparison, this rate was less than the value of 0.17 nm/cycle, as observed using this same pulse sequence for substrates maintained at 250 °C.[34,35] Permalloy deposition was done by molecular beam deposition from an alloy source at normal incidence at a rate of 3 nm/min with a source-to-substrate distance of 72 cm, a growth pressure of roughly 0.5 to 1.3 × 10^{-8} Torr, and a substrate temperature of 23−27 °C. Nanostructure patterning was done *via* Ar ion beam milling (beam current 80 mA, accelerating voltage 100 V, 8 × 10^{-5} Torr of Ar) at normal incidence.

Scanning electron microscopy was performed on a Hitachi S900 FE-SEM using an accelerating voltage between 2.0 and 5.0 kV. Polymer films were coated with an ~3 nm layer of Pt across the surface prior to imaging to avoid charging; other structured films were imaged without any processing. Layer thicknesses (permalloy and ZnO) were determined with grazing incidence X-ray reflectivity on a Panalytical X'Pert Pro with a Cu Kα source. Resonance enhanced Rutherford backscattering spectrometry (RERBS), using a 3.00 MeV He^+ beam to increase the sensitivity toward oxygen, established that the as-deposited films were oxygen rich (O/Zn = 1.5). It is likely that the extra oxygen is associated with the presence of hydroxide. X-ray diffraction of the ZnO film was performed on a silicon wafer. Direct current magnetometry measurements were carried out using a Quantum Design superconducting quantum interference device (SQUID) magnetometer from 20 to 300 K.

Conflict of Interest: The authors declare no competing financial interest.

Acknowledgment. Work was supported primarily by the National Science Foundation (NSF) through the University of Minnesota MSREC under Award Number DMR-0819885 and DMR-1420013. Parts of this work were carried out in the Characterization Facility, University of Minnesota, which receives partial support from the NSF through the MRSEC program, as well as the Minnesota Nano Center.

Supporting Information Available: X-ray reflectivity and diffraction patterns of ZnO films, details of the SEM image analysis process used to calculate pore and nanodot diameters, and SEM images showing the time dependence of the Ar ion milling process and tilted cross-sectional views are included. This material is available free of charge *via* the Internet at http://pubs.acs.org.

REFERENCES AND NOTES

1. Bang, J.; Jeong, U.; Ryu, D. Block Copolymer Nanolithography: Translation of Molecular Level Control to Nanoscale Patterns. *Adv. Mater.* **2009**, *21*, 4769–4792.
2. Hamley, I. Ordering in Thin Films of Block Copolymers: Fundamentals to Potential Applications. *Prog. Polym. Sci.* **2009**, *34*, 1161–1210.
3. Lazzari, M.; López-Quintela, M. A. Block Copolymers as a Tool for Nanomaterial Fabrication. *Adv. Mater.* **2003**, *15*, 1583–1594.
4. Thurn-Albrecht, T.; Steiner, R.; DeRouchey, J.; Stafford, C. M.; Huang, E.; Bal, M.; Tuominen, M.; Hawker, C. J.; Russell, T. P. Nanoscopic Templates from Oriented Block Copolymer Films. *Adv. Mater.* **2000**, *12*, 787–791.
5. Ruiz, R.; Kang, H.; Detcheverry, F. A.; Dobisz, E.; Kercher, D. S.; Albrecht, T. R.; de Pablo, J. J.; Nealey, P. F. Density Multiplication and Improved Lithography by Directed Block Copolymer Assembly. *Science* **2008**, *321*, 936–939.
6. Park, S.; Wang, J.-Y.; Kim, B.; Xu, J.; Russell, T. P. A Simple Route to Highly Oriented and Ordered Nanoporous Block Copolymer Templates. *ACS Nano* **2008**, *2*, 766–772.
7. Luo, M.; Epps, T. H., III. Directed Block Copolymer Thin Film Self-Assembly: Emerging Trends in Nanopattern Fabrication. *Macromolecules* **2013**, *46*, 7567–7579.
8. Ramanathan, M.; Tseng, Y.-C.; Ariga, K.; Darling, S. B. Emerging Trends in Metal-Containing Block Copolymers: Synthesis, Self-Assembly, and Nanomanufacturing Applications. *J. Mater. Chem. C* **2013**, *1*, 2080–2091.
9. Bates, C. M.; Maher, M. J.; Janes, D. W.; Ellison, C. J.; Wilson, C. G. Block Copolymer Lithography. *Macromolecules* **2014**, *47*, 2–12.
10. Bates, F. S. Polymer-Polymer Phase Behavior. *Science* **1991**, *251*, 898–905.
11. Cheng, J. Y.; Ross, C. A.; Chan, V. Z.-H.; Thomas, E. L.; Lammertink, R. G. H.; Vancso, G. J. Formation of a Cobalt Magnetic Dot Array via Block Copolymer Lithography. *Adv. Mater.* **2001**, *13*, 1174–1178.
12. Bandić, Z. Z.; Litvinov, D.; Rooks, M. Nanostructured Materials in Information Storage. *MRS Bull.* **2008**, *33*, 831–837.
13. Ross, C. A.; Cheng, J. Y. Patterned Magnetic Media Made by Self-Assembled Block Copolymer Lithography. *MRS Bull.* **2008**, *33*, 838–845.
14. Griffiths, R. A.; Williams, A.; Oakland, C.; Roberts, J.; Vijayaraghavan, A.; Thomson, T. Directed Self-Assembly of Block Copolymers for Use in Bit Patterned Media Fabrication. *J. Phys. D: Appl. Phys.* **2013**, *46*, 503001–503030.
15. Thurn-Albrecht, T.; Schotter, J.; Kästle, G. A.; Emley, N.; Shibauchi, T.; Krusin-Elbaum, L.; Guarini, K.; Black, C. T.; Tuominen, M. T.; Russell, T. P. Ultrahigh-Density Nanowire Arrays Grown in Self-Assembled Diblock Copolymer Templates. *Science* **2000**, *290*, 2126–2129.
16. Jung, Y. S.; Ross, C. A. Orientation-Controlled Self-Assembled Nanolithography Using a Polystyrene−Polydimethylsiloxane Block Copolymer. *Nano Lett.* **2007**, *7*, 2046–2050.
17. Stoykovich, M. P.; Kang, H.; Daoulas, K. C.; Liu, G.; Liu, C.-C.; de Pablo, J. J.; Müller, M.; Nealey, P. F. Directed Self-Assembly of Block Copolymers for Nanolithography: Fabrication of Isolated Features and Essential Integrated Circuit Geometries. *ACS Nano* **2007**, *1*, 168–175.
18. Black, C. T. Polymer Self-Assembly as a Novel Extension to Optical Lithography. *ACS Nano* **2007**, *1*, 147–150.
19. Tang, C.; Lennon, E. M.; Fredrickson, G. H.; Kramer, E. J.; Hawker, C. J. Evolution of Block Copolymer Lithography to Highly Ordered Square Arrays. *Science* **2008**, *322*, 429–432.
20. Peng, Q.; Tseng, Y.-C.; Darling, S. B.; Elam, J. W. Nanoscopic Patterned Materials with Tunable Dimensions via Atomic Layer Deposition on Block Copolymers. *Adv. Mater.* **2010**, *22*, 5129–5133.
21. Peng, Q.; Tseng, Y.-C.; Darling, S. B.; Elam, J. W. A Route to Nanoscopic Materials via Sequential Infiltration Synthesis on Block Copolymer Templates. *ACS Nano* **2011**, *5*, 4600–4606.
22. Tseng, Y.-C.; Peng, Q.; Ocola, L. E.; Elam, J. W.; Darling, S. B. Enhanced Block Copolymer Lithography Using Sequential Infiltration Synthesis. *J. Phys. Chem. C* **2011**, *115*, 17725–17729.

23. Tseng, Y.-C.; Peng, L. E.; Ocola, L. E.; Czaplewski, D. A.; Elam, J. W.; Darling, S. B. Enhanced Polymeric Lithography Resists via Sequential Infiltration Synthesis. *J. Mater. Chem.* **2011**, *21*, 11722–11725.
24. Tseng, Y.-C.; Mane, A. U.; Elam, J. W.; Darling, S. B. Enhanced Lithographic Imaging Layer Meets Semiconductor Manufacturing Specification a Decade Early. *Adv. Mater.* **2012**, *24*, 2608–2613.
25. Xiao, S.; Yang, X.; Edwards, E. W.; La, Y.-H.; Nealey, P. F. Graphoepitaxy of Cylinder-Forming Block Copolymers for Use as Templates to Pattern Magnetic Metal Dot Arrays. *Nanotechnology* **2005**, *16*, S324–S329.
26. Sinturel, C.; Vayer, M.; Morris, M.; Hillmyer, M. A. Solvent Vapor Annealing of Block Polymer Thin Films. *Macromolecules* **2013**, *46*, 5399–5415.
27. Baruth, A.; Seo, M.; Lin, C.-H.; Walster, K.; Shankar, A.; Hillmyer, M. A.; Leighton, C. Optimization of Long-Range Order in Solvent Vapor Annealed Poly(styrene)-*block*-poly(lactide) Thin Films for Nanolithography. *ACS Appl. Mater. Interfaces* **2014**, *6*, 13770–13781.
28. Baruth, A.; Rodwogin, M. D.; Shankar, A.; Erickson, M. J.; Hillmyer, M. A.; Leighton, C. Non-Lift-off Block Copolymer Lithography of 25 nm Magnetic Nanodot Arrays. *ACS Appl. Mater. Interfaces* **2011**, *3*, 3472–3481.
29. Olayo-Valles, R.; Lund, M. S.; Leighton, C.; Hillmyer, M. A. Large Area Nanolithographic Templates by Selective Etching of Chemically Stained Block Copolymer Thin Films. *J. Mater. Chem.* **2004**, *14*, 2729–2731.
30. Moon, H.-S.; Kim, J. Y.; Jin, H. M.; Lee, W. J.; Choi, H. J.; Mun, J. H.; Choi, Y. J.; Cha, S. K.; Kwon, S. H.; Kim, S. O. Atomic Layer Deposition Assisted Pattern Multiplication of Block Copolymer Lithography for 5 nm Scale Nanopatterning. *Adv. Funct. Mater.* **2014**, *24*, 4343–4348.
31. George, S. M. Atomic Layer Deposition: An Overview. *Chem. Rev.* **2010**, *110*, 111–131.
32. Elam, J. W.; Routkevitch, D.; Mardilovich, P. P.; George, S. M. Conformal Coating on Ultrahigh-Aspect-Ratio Nanopores of Anodic Alumina by Atomic Layer Deposition. *Chem. Mater.* **2003**, *15*, 3507–3517.
33. Kumagai, H.; Kusunoki, T.; Kobayashi, T. Surface Modification of Polymers by Thermal Ozone Treatments. *AZojomo [Online]* **2007**, 10.2240/azojomo0246.
34. Warner, E. J.; Cramer, C. J.; Gladfelter, W. L. Atomic Layer Deposition of ZnO: Understanding the Reactions of Ozone with Diethylzinc. *J. Vac. Sci. Technol. A* **2013**, *31*, 415041–415047.
35. Yuan, H.; Luo, B.; Yu, D.; Cheng, A.-j.; Campbell, S. A.; Gladfelter, W. L. Atomic Layer Deposition of Al-Doped ZnO Films Using Ozone as the Oxygen Source: A Comparison of Two Methods to Deliver Aluminum. *J. Vac. Sci. Technol., A* **2012**, *30*, 1A1381–1A1388.
36. Ross, C. A.; Hwang, M.; Shima, M.; Cheng, J. Y.; Farhoud, M.; Savas, T. A.; Smith, H. I.; Schwarzacher, W.; Ross, F. M.; Redjahl, M.; Humphrey, F. B. Micromagnetic Behavior of Electrodeposited Cylinder Arrays. *Phys. Rev. B* **2002**, *65*, 1444171–1444178.
37. Scholz, W.; Guslienko, K.Yu; Novosad, V.; Suess, D.; Schrefl, T.; Chantrell, R. W.; Fidler, J. Transition from Single-Domain to Vortex State in Soft Magnetic Cylindrical Nanodots. *J. Mag. Mag. Mater.* **2003**, *266*, 155–163.
38. Dumas, R. K.; Liu, K.; Li, C.-P.; Roshschin, I. V.; Schuller, I. K. Temperature Induced Single Domain-Vortex State Transition in Sub-100 nm Fe Nanodots. *Appl. Phys. Lett.* **2007**, *91*, 2025011–2025013.